Experimental Study of the Micromechanical Behavior of Ferrite in DP Steel Under Various Stress States

YONGSHENG XU, WENJIAO DAN, CHUANWEI LI, and WEIGANG ZHANG

The low yield ratio and continuous yielding behavior of ferrite-martensite dual-phase (DP) steels are determined by their production process and microstructure. In this work, high-resolution *in situ* electron backscatter diffraction (EBSD) experiments were performed to study the deformation and hardening behavior of DP steel in uniaxial tensile, plane strain and shear stress states. In the EBSD experiments, we first collected the data for different deformation stages from the same area for each sample (loading was paused during EBSD data collection). Subsequently, we analyzed the strain contouring maps, geometrically necessary dislocation (GND) distribution and ferrite deformation of all the samples based on the postprocessing of the EBSD data. The results showed that (i) the volume expansion accompanying the austenite-to-martensitic transformation during annealing gives rise to ferrite plastic deformation, and the residual deformation after overaging of the fine ferrite grains near the martensite group is the largest; (ii) the high-density GND bands of the shear sample is the same as the shear stress/strain direction, and the high-density GND bands of the uniaxial tensile and plane strain samples are perpendicular to their maximum stress/strain directions; and (iii) in the shear state, the average strain of ferrite grains in each grain size range is similar; but the deformation tends to aggregate toward large-size grains in the uniaxial tensile and plane strain samples.

https://doi.org/10.1007/s11661-020-05867-1
© The Minerals, Metals & Materials Society and ASM International 2020

I. INTRODUCTION

FERRITE-MARTENSITE dual-phase (DP) steels are multiphase materials composed of soft ferrite and hard martensite that are widely used for their good mechanical properties and low manufacturing cost.[1–3] Generally, DP steels are produced by one of two approaches[4]; the first approach is to use a hot rolling method that obtains a two-phase structure of ferrite and martensite by controlling the final rolling temperature and cooling rate.[5,6] This method has clear advantages with regard to energy consumption and is suitable for producing thicker plates. The second approach is to use a cold rolling method, in which a two-phase structure is obtained by subjecting the rolled sheets to intercritical annealing.[5,7–9] During the annealing (typical heat treatment process illustrated in Figure 1), the steel sheets are first be heated to the ferrite and austenite two-phase regions and then are soaked, followed by rapid cooling to promote the austenite-to-martensite transformation. This method exhibits a high production efficiency and is used in a wide range of applications. The phase transition is similar in both the hot rolling and the cold rolling process; that is, the martensite phase is obtained by rapid cooling.

The crystal structure transformation (face-centered cubic (FCC) to body-centered tetragonal (BCT)) and supersaturated carbon atoms give rise to a decrease in the efficiency of space-filling of the martensite unit cell and a volume expansion of the phase transition region.[10,11] The volume expansion causes plastic deformation and initial hardening of the ferrite near the phase boundary; the hardening effect becomes more significant as the martensite volume fraction increases and the grain size decreases.[10] Various studies have shown that the residual deformation after annealing of ferrite makes the elastic limit and yield strength of DP steels much lower than those of the sample prior to quenching (quenching gives rise to residual stress and high-density movable dislocations in DP steels).[11] Tsipouridis et al.[12] noted that the average dislocation density of ferrite in DP steels was dependent on the volume fraction of martensite and that the high-density dislocation resulted in continuous yielding behavior of DP steels.[13,14] In summary, the dual-phase microstructure

YONGSHENG XU, WENJIAO DAN, and WEIGANG ZHANG are with the Department of Engineering Mechanics, School of Naval Architecture, Ocean and Civil Engineering, Shanghai Jiao Tong University, Shanghai 200240, China. Contact e-mail: wjdan@sjtu.edu.cn CHUANWEI LI is with the Institute of Materials Modification and Modeling, School of Materials Science and Engineering, Shanghai Jiao Tong University, Shanghai, 200240, China. Contact e-mail: li-chuanwei@sjtu.edu.cn

Manuscript submitted August 20, 2019.

Published online: 14 June 2020

and the initial hardening characteristics of ferrite determine the macroscopic mechanical behavior of DP steels.

On the other hand, due to the huge difference in the mechanical properties of ferrite and martensite, the partitioning and matching of ferrite and martensite strain during the deformation of DP steel sheets have attracted much research interest. The strain inhomogeneity of DP steels was studied by electron backscatter diffraction (EBSD), scanning electron microscope (SEM), and micro-digital image correlation (μ-DIC) methods, and these results showed that the ferrite strain was much larger than that of martensite.[15–20] In addition, the ferrite strain maps indicated that the ferrite strain is also strongly inhomogeneous and is related to its adjacent martensite distribution; further, the strain of ferrite between the martensite blocks is higher than the average ferrite strain.[17–20]

In DP steels, the regions near the phase boundary of ferrite play a bridging role in the deformation and strength mismatch of two phases. Lattice mismatch in the vicinity of martensite results in a large number of geometrically necessary dislocations (GNDs) in this region to maintain lattice continuity.[10,11,16,20] The dislocation-based hardening model emphasizes that the material strength increases with higher dislocation density (including GND and statistically stored dislocation (SSD)).[10,21,22] Therefore, the high-density dislocations in the vicinity of martensite increase the strength of these regions, and nanoindentation experiments also indicated that these regions are harder than the ferrite center area.[23,24] Moreover, the strain gradient caused by the strain heterogeneity of DP steel increases the GND density during deformation.[25,26]

In this work, the microstructure of DP steel and the evolution of its micromechanical behavior under various stress states were studied with the *in situ* EBSD method. For the EBSD experiments, we designed stretching samples for three stress states, namely, shear, uniaxial tension, and plane strain. Then, we analyzed the effect of martensite transformation on the residual deformation and hardening of ferrite. Finally, the distribution characteristics of GND and ferrite deformation under various stress states and their evolution with stretching deformation were analyzed.

II. MATERIAL AND EXPERIMENTS

A. *Material*

The steel sheets studied in this paper were a commercial grade DP780 dual-phase steel, and the chemical composition is listed in Table I. These steel sheets were formed by cold rolling and continuous annealing to a thickness of 0.8 mm. We performed the uniaxial tensile test on DP780 steel at a strain rate of 0.001/s, and the obtained engineering stress-strain curves are shown in Figure 2(a). After polishing and etching, one of metallographs of the steel sheet is shown in Figure 2(b). The metallograph shows that this steel sheet consisted of ferrite and martensite (dark etched region in the figure) phases, in which the average ferrite grain size is 5 μm and the martensite volume fraction is approximately 28 pct (use the image processing code to calculate the martensite volume fraction based on the grayscale difference of ferrite and martensite).

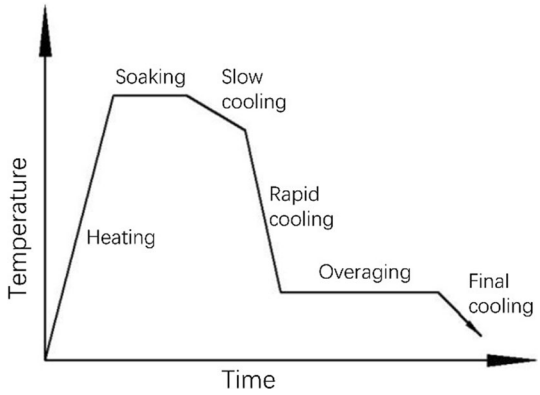

Fig. 1—Typical schematic diagram of intercritical annealing for DP steels.

B. *Samples*

To explore the grain deformation and hardening features of DP steel under various stress states, we designed three type of samples suitable for EBSD *in situ* stretching tests (as shown in Figure 3), which are corresponding to the uniaxial tensile, plane strain and shear stress states. All of the samples were cut from the same steel sheet by using wire electrical discharge machining (WEDM), and the stretching direction of samples is parallel to their rolling direction. For these three stress state samples (based on the EBSD test requirements, the thickness of the polished samples is 0.6 mm), the ABAQUS was used to perform a finite element simulation of the stretching tests. The strain component-equivalent plastic strain curves of each sample are shown in Figures 4(a) through (c). In the middle region of these samples, the shear deformation (γ_{12}) of shear sample is the main part, and the normal strains (ε_{11}, ε_{22}, and ε_{33}) are almost 0 (Figure 4(a)); the transverse strain (ε_{22}) of the uniaxial tensile sample is close to the thickness direction strain (ε_{33}), which is about -0.5 times that of the tensile strain (ε_{11}) (Figure 4(b)); the transverse strain (ε_{22}) of plane strain sample is close to 0, and the middle area is obviously thinned (Figure 4(c)). In addition, the stress triaxiality-equivalent plastic strain curves also show that the stress state in the middle region of the three samples is consistent with expectations (Figure 4(d)).

For EBSD experiments, to eliminate the residual deformation caused by polishing, the samples were first ground using wet sandpaper (the finest sandpaper is 3000 mesh), and then, all of the samples were polished by vibratory polishers to meet the requirements of EBSD experiment.

Table I. Chemical Composition of DP780 Steel

Element	C	Cr	Cu	Mn	Mo	Ni	P	Si	S
Content (Wt Pct)	0.1658	0.0347	0.006	1.514	0.0096	0.027	0.0123	0.1821	0.00172

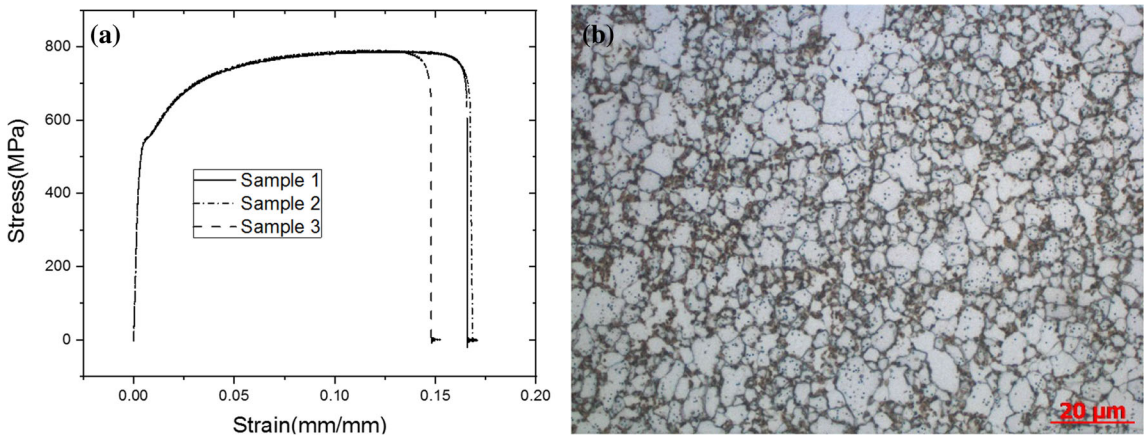

Fig. 2—The engineering stress-strain curves (*a*) and undeformed metallograph (*b*) of DP780 steel.

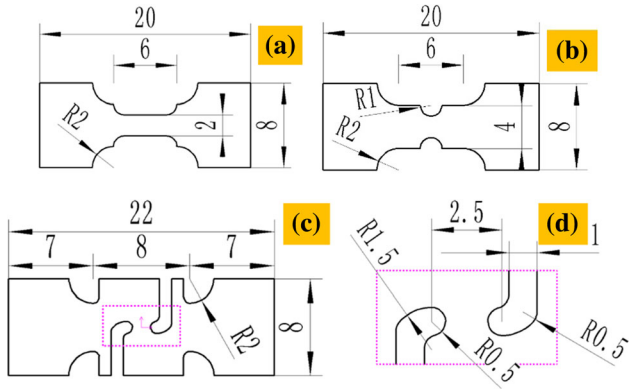

Fig. 3—Samples for *in situ* EBSD experiment. (*a*) Uniaxial tensile sample; (*b*) plane strain sample; (*c*) shear sample; (*d*) the zoomed region of shear sample.

C. *EBSD Experiments*

The EBSD data were obtained using a high-resolution field emission scanning electron microscopy (FE-SEM) system with an EBSD module (LYRA3 GAU, TESCAN, angular resolution is 0.05 deg). Diffraction patterns were collected through a high-speed charge-coupled device (CCD) module, and all the experiments were performed at a step size of 100 nm. In the EBSD experiment, the electron acceleration voltage was 20 kv and the current was 5 nA. The sample was tilted at an angle of 70 deg with a pitch of 14.5 mm. The laboratory temperature was 23 °C and the humidity was 60 pct.

We first performed EBSD data acquisition on the undeformed sample, then used an internal stretcher to stretch the sample, and again performed data acquisition on the same area during the stretching pause. We collected four sets of EBSD data for the different strains of each sample. Since the quality of the diffraction pattern of martensite is lower than that of ferrite, the ferrite and martensite were distinguished according to the difference of gray scale of the band contrast (BC) maps.

III. RESULTS AND DISCUSSION

A. *Residual Deformation and Hardening After Annealing of Ferrite*

The martensite transformation in the annealing process (MTAP) determines the final microstructure of the DP780 steel sheet. To characterize the effect of MTAP on the adjacent ferrites, the residual deformation caused by the phase transition was measured based on the lattice distortion of the ferrite in the undeformed samples. Based on the characteristics of ferrite residual deformation, the effect of the martensite distribution, local martensite volume fraction (LMVF), and ferrite grain size on the residual deformation of ferrite was analyzed. In this work, CHANNEL 5 and OIM Analysis 5.3 software were used to calculate the lattice distortion feature of ferrite. Strain contouring (SC, the component measures the maximum misorientation between any 2 points in a grain and then weights this grain according to this misorientation value) maps were used to quantify the residual deformation of ferrite. The SC map provides an estimate of deformation or strain in individual grains in a map. Although its magnitude is not a traditionally defined strain,[27–29] it is appropriate to qualitatively analyze the correlation between the microstructure of DP steel and the residual deformation in the micro-region.

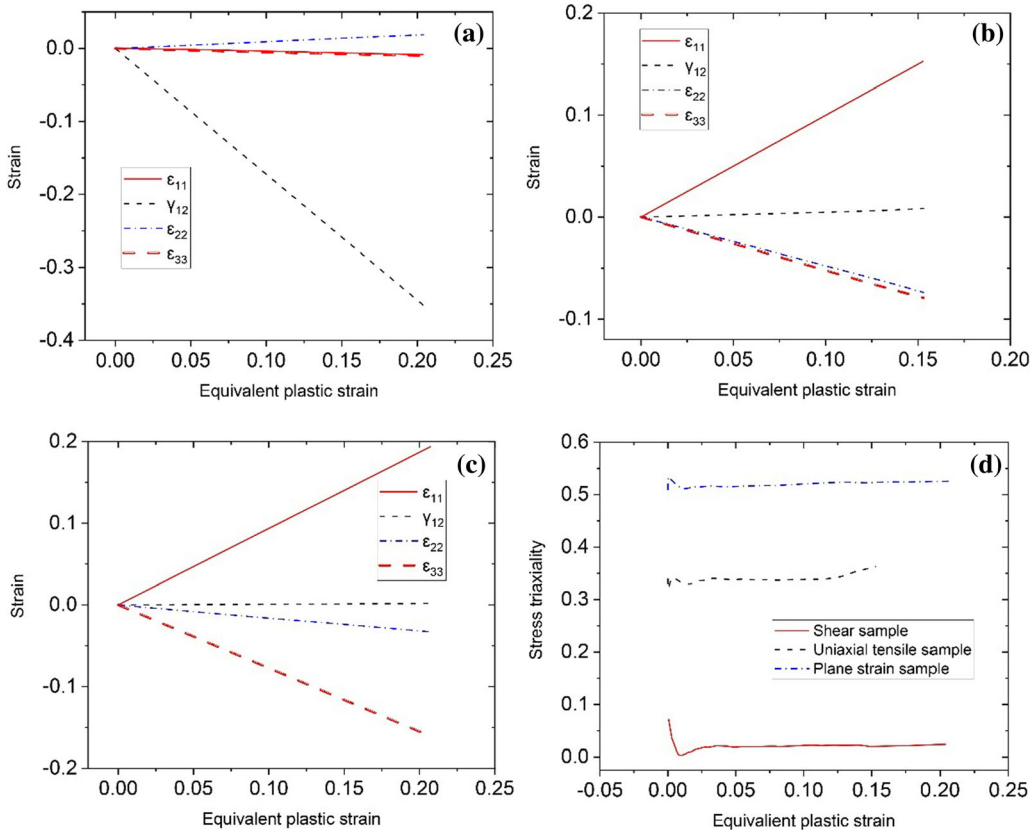

Fig. 4—Strain component and stress triaxiality in the center deformation zone of different stress state samples. (*a*) The strain component of shear condition; (*b*) the strain component of uniaxial tensile condition; (*c*) the strain component of plane strain condition; (*d*) the stress triaxiality of all samples.

Figures 5(a1) through (c1) show the SC maps of the three undeformed samples, the magnitude of which reflects the residual deformation of these regions. Figures 5(a2) through (c2) are the corresponding LMVF maps, representing the martensite area ratio in the square area with appropriate width around the pixel (the width in this maps is the average ferrite grain size, 5 μm). Figures 5(a3) through (c3) show the IPF-Z maps of the same region that are used to characterize the grain size and orientation more clearly. In addition, the detailed information of the marked grains in Figure 5 is shown in Table II.

The ferrite residual deformation is the largest in the area indicated by the red ellipse in the SC maps (Figures 5(a1) through (c1)), where the martensite is the densest. The volume expansion caused by MTAP exerts greater internal stress on the surrounding ferrites, resulting in the plastic deformation of ferrites in these regions. On the contrary, in the region where the martensite is sparse, the ferrite is less affected by the phase transition and does not show any noticeable plastic deformation (as shown by the gray ellipse in Figure 5(a1)). Compared with LMVF maps (Figures 5(a2) through (c2)), it can be seen that the LMVF in the high residual strain regions is greater than 30 pct. In addition, comparison with IPF maps (Figures 5(a3) through (c3)) show that the residual strain is independent of the orientation of the ferrite.

The ferrite grain size of DP780 was divided into five groups (grain size ranges: 0 to 2, 2 to 3, 3 to 4, 4 to 5, and 5 to 10 μm), and the relationship between the LMVF and the grain size is calculated, as shown in Figure 6. The results show that ferrite with a grain size of less than 3 μm has the highest LMVF, indicating that the small-size ferrite has the largest residual deformation. Figures 5(a2) through (c2) and Figure 6 show that the ferrite grains in the martensite-rich region are fine, and the ferrite grains far from the martensite-rich region have the largest grain size. The two grains in the area surrounded by the purple circle in Figure 5(c1) are close to the rich-martensite region, but the deformation of the small grain is significantly larger than the large grain. In addition, for ferrite with similar grain size, the residual deformation increases with the higher local martensite volume fraction (such as B1 and B2 in Figure 5(b1), and C1 and C2, C3 and C4 in Figure 5(c1)).

On the other hand, the effect of martensite distribution on the residual deformation of ferrite is also significant. The intragranular residual deformation of ferrite grains shown in B5, B6, C1, C3, and C4 in Figure 5 is the same, and the martensite distribution in the corresponding regions shows good uniformity. On the contrary, for ferrites with martensite concentrated in part of the grain boundaries (such as A1 to A5 in Figure 5(a1), B7 to B9 in Figure 5(b1), and C1, C5, and C6 in Figure 5(c1)), the residual deformation in the

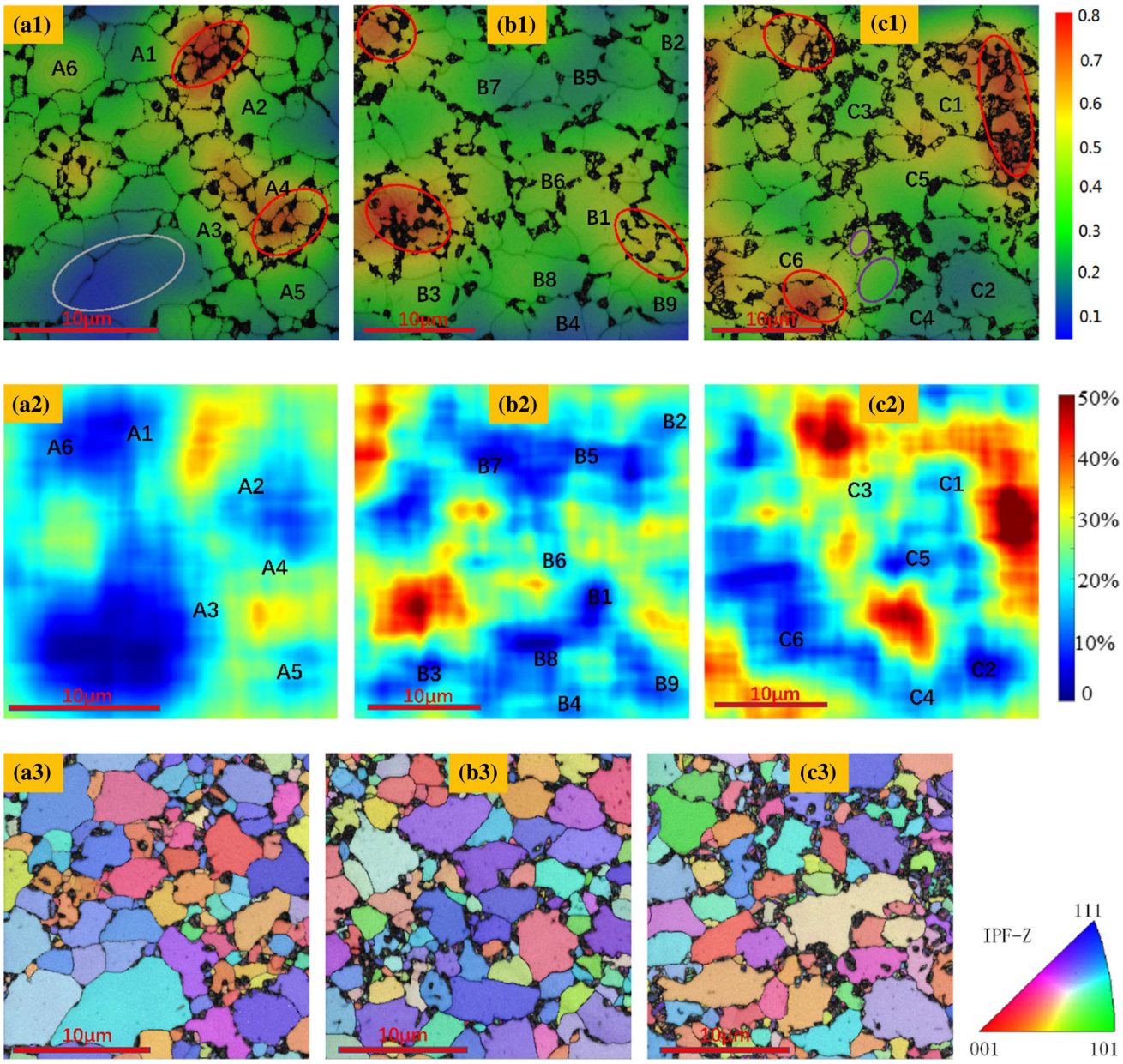

Fig. 5—The micro-features of undeformed samples. (*a1*), (*b1*), and (*c1*) are the SC map of shear sample, uniaxial tensile sample ,and plane strain sample, respectively; (*a2*), (*b2*), and (*c2*) are the local martensite volume fraction (LMVF) map of shear sample, uniaxial tensile sample, and plane strain sample, respectively; (*a3*), (*b3*), and (*c3*) are the inverse pole figure-Z (IPF-Z) map of shear sample, uniaxial tensile sample, and plane strain sample, respectively.

ferrite grains is unevenly distributed, and it decreases with increasing distance from the phase boundary. In Figure 5(a1), a special phenomenon occurs in the A6 region, where the residual deformation in the middle region of ferrite is larger than that in the phase boundary. We suspect that this abnormality is caused by the inhomogeneous martensite distribution in the thickness direction.

The inhomogeneity of residual deformation results in an uneven distribution of the initial work hardening of ferrite. Unfortunately, the micromechanical differences are prone to strain concentration and microcracking in DP steel that reduce its elongation. In short, the uneven distribution of martensite at the grain boundaries leads to nonuniform intragranular residual deformation of large-size ferrite. The difference in grain size is also caused by the local enrichment of martensite, which makes the intergranular residual deformation of ferrite significantly different. For cold-rolled dual-phase steel, the intercritical annealing is the process that determines its microstructure. Promoting the uniformity of the martensite distribution will help reduce the difference in the initial hardening of the micro-region of the dual-phase steel and improve its ductility.

Moreover, the GND is also an important factor affecting DP steel initial hardening. GND maps (Figures 7(a1) through (c1)) of undeformed samples were calculated with the kernel average misorientation (KAM) method.[10,11,24] The relationship between KAM (θ) and GND density (ρ_{GND}) is as follows,

$$\rho_{GND} = \frac{2\theta}{ub}$$

where u is the unit length, and b is the magnitude of the Burgers vector. As a first order approach, the KAM, which is retrieved directly from EBSD data.

In this paper, the neighbor unit length was set to 300 nm, the maximum misorientation angle was 5 deg. GND maps show that the high GND density (4.6×10^{14} m^{-2}) regions are distributed around the grain/phase boundary, and the width of the high-value region is 100 to 500 nm. The results were also shown by the hardness test.[24] The above analysis shows that GND plays a major role in bridging the difference in the orientation between different grains to ensure the continuity at the interface. The lattice mismatch of ferrite caused by MTAP is mild or gradual within the ferrite and does not result in the ferrite lattice curvature. Meanwhile, a comparison of GND maps (Figures 7(a1) through (c1)) and SC maps (Figures 5(a1) through (c1)) shows that although MTAP leads to a noticeable residual plastic deformation of some ferrites, it has little effects on the GND distribution in the same region after overaging. We speculate that the lattice curvature inside the ferrite grains is easier to recover during overaging, while the statistical storage dislocation (SSD) related to plastic deformation are partially retained.

B. *GND Evolution Under Various Stress States*

Plastic deformation reduces the quality of the diffraction pattern, and excessive deformation makes the EBSD data unusable. Therefore, GND maps of three deformation stages were selected to study the GND evolution under various stress states. The maximum shear strain of the shear sample was 0.19, the maximum tensile strain of the uniaxial tensile sample was 0.12, and the maximum tensile strain of the plane strain sample was 0.11. To quantify the deformation of each sample, we calculated the von-Mises equivalent strain (E-strain) of the three samples according to the principal strain of each sample and its stress state, which are presented in Table III.

Figure 7 shows the evolution and distribution maps of GND with deformation under uniaxial tensile, plane strain and shear stress states. As shown in Figure 7, the expansion of the dark regions with increasing deformation indicates the presence of a high strain gradient and severe lattice distortion at the phase boundary.[30] The GND caused by the high strain gradient bridges the strain difference between ferrite and martensite.

These results (Figure 7) also indicate that the stress state plays an important role in the GND generation and evolution of DP steel. In shear condition, martensite acts as a hard particle to hinder the shear deformation of ferrite (Figure 7(a)), and the high-density GND bands appear on one side of martensite (such as the areas marked by the red circle in Figure 7(a)). In addition, the high-density GND bands within the ferrite of the shear sample present horizontal and vertical patterns consistent with the shear stress/strain direction. For uniaxial tensile and plane strain conditions (Figures 7(b) and (c)), the ferrite GND in the regions between the martensite blocks increases most rapidly (such as the areas marked by the red circles in Figures 7(b) and (c)), and as the strain increases, the high-density GND regions of ferrite present a long strip perpendicular to the direction of the tensile strain (Figures 7(b3) and (c3)). The high-density GND bands first form at the ferrite phase/grain boundary, and then go deep into the ferrite with increasing strain. On the other hand, the grains of the uniaxial tensile sample not only elongate along the stretching direction but also shrink in the transverse direction with increasing deformation. Therefore, the transverse strain gradient will generate some horizontal high-density GND bands in the ferrite (such as the areas shown by the blue arrow in Figure 7(b3)). However, due to the lateral strain constraint (almost equal to 0), the high-density GND bands of the ferrite in the plane strain sample are almost perpendicular to the stretching direction (Figure 7(c3)).

The stress state in the deformation region determines the distribution features of the high-density GND region. Due to the huge strength difference between ferrite and martensite, the ferrite between the martensite blocks deforms violently at first and has a high strain gradient. With increasing deformation, the high deformation gradient zone will penetrate deep into the ferrite, eventually leading to the formation of high-density GND bands in the ferrite (Figure 7).

To quantitatively analyze the effect of macro-deformation on the evolution of the ferrite GND density of DP steel, the GND density of ferrite with different grain sizes after deformation was calculated, as shown in Figure 8. The results show that plastic deformation causes a rapid increase in the average GND density of ferrite (Figures 8(a) through (c)). When the equivalent strains of the three samples are approximately equal to 0.12, the average GND density reaches 2.5 to 4 times the initial density.

The initial average GND density of ferrite is approximately 1.8×10^{14} (m^{-2}), and the average GND density first increases and then decreases with increasing grain size (Figure 8(d)). The average GND density is highest when the grain size is 2-3 μm and decreased rapidly when the grain size is larger than 4 μm. A comparison of Figures 5(a3) through (c3) and Figures 7(a1) through (c1) shows that the fine ferrite grains (grain size less than 3 μm) are concentrated around the martensite cluster and have the highest GND density. The increase in the grain/phase boundary caused by the decrease in the grain size and the plastic deformation caused by MTAP are the main reasons for the high average GND density of fine ferrites. However, when the grain size is less than 2 μm, the average GND density of ferrite does not increase as the increase of the grain boundaries, indicating that the martensite volume expansion does not

Table II. The Grain Size, LMVF, and Orientation of the Ferrite Grains in the Marked Areas

Grain ID \Item	LMVF (Pct)	Grain Size (μm)	Euler Angle (Bunge, degree)	Grain ID \Item	LMVF (Pct)	Grain Size (μm)	Euler Angle (Bunge, degree)
A1	26.3	4.4	(243.6 20.2 33.8)	B6-1	33.7	4.2	(163.7 45.9 51.4)
A2	31.4	4.0	(30.9 4.0 23.1)	B6-2	34.1	3.1	(163.6 50.9 44.5)
A3	31.8	3.8	(98.3 37.1 45.8)	B7	15.3	6.5	(48.6 38.2 50.1)
A4	42.8	3.5	(45.1 19.8 78.4)	B8	19.6	7.0	(198.3 51.0 42.3)
A5	36.1	4.5	(65.8 46.6 44.9)	B9	22.8	4.6	(170.0 37.5 34.4)
A6	25.1	6.1	(271.6 46.6 33.9)	C1	27.8	5.3	(178.1 44.1 41.2)
B1	18.8	6.0	(357.3 18.5 59.0)	C2	5.1	7.2	(293.9 34.7 30.2)
B2	25.5	4.9	(347.2 14.2 40.5)	C3	35.7	4.4	(148.8 46.0 66.9)
B3	20.0	5.5	(258.0 41.2 39.6)	C4	26.7	4.7	(141.4 47.7 65.5)
B4	23.1	4.7	(291.6 39.9 51.7)	C5	22.0	7.9	(261.9 27.9 19.4)
B5-1	31.4	4.4	(35.1 16.7 2.2)	C6	15.7	6.4	(45.1 20.6 77.5)
B5-2	33.3	3.8	(200.7 44.0 37.7)				

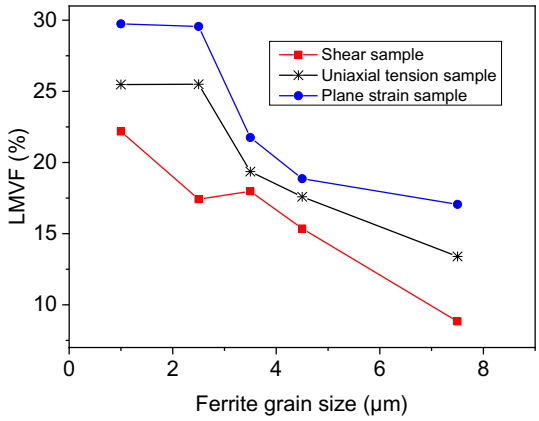

Fig. 6—The LMVF-ferrite grain size curves of undeformed samples.

give rise to a severe lattice curvature of the finest ferrite grains.

Figure 8(e) shows the relationship between the GND density and the grain size caused by the deformation of the three stress state samples. The corresponding initial density is subtracted from the average GND density after deformation of the sample to characterize the effect of deformation on the evolution of GND. The results show that, except for the finest grains (grain size less than 2 μm), the increase in the average GND density caused by deformation is less related to the grain size, and the increase in the GND density in each size range of a sample is similar. However, the amount of the GND increase caused by the deformation depends on the stress state. That is, for the same equivalent strain, the GND increment of the shear sample is greater than those of the uniaxial tensile and plane strain samples (Figures 8(e) and (f)).

C. *Effect of Stress State on Ferrite Deformation*

The microstrain of the DP steels is inhomogeneous, and the ferrite strain is clearly higher than that of martensite. Plastic deformation leads to a decrease in the quality of the diffraction pattern, which is mainly due to the deterioration of the flatness of the sample (caused by grain rotation and strain concentration) and the lattice distortion caused by the deformation. The correlation between lattice distortion and deformation provides an effective approach to measure the plastic deformation of a grain by measuring its local misorientation,[31–35] such as by using the grain orientation spread (GOS), the kernel average neighbor misorientation (KANM), etc. Although local misorientation does not give an accurate strain field, it can qualitatively describe the distribution of deformation of the grain. In this section, we analyze the influence of the stress state on ferrite deformation according to GOS calculated by EBSD data, as shown in Figure 9.

Figures 9(a1) through (c1) show the GOS maps of undeformed samples. These figures show that the initial GOS of most grains is less than 0.5 deg, and the high-value regions are mostly concentrated near the martensite cluster. This phenomenon also indicates that the ferrite in the vicinity of the martensite has the largest residual plastic deformation. As the deformation increases, the GOS of the large-size grains increases most rapidly (Figure 9), indicating that the large-size ferrite grains have weaker initial hardening and are more susceptible to deformation.

Figure 10 quantitatively describes the relationship between the deformation and GOS of each sample. Figure 10(a) shows the relationship between the average GOS and the equivalent strain under different stress states. The results show that the average GOS increases linearly with increasing equivalent strain[32]. However, the slopes of GOS-equivalent strain curve are not completely consistent, and the highest slope is observed for the uniaxial tensile condition. When the grain size is in the range of 2 to 3 μm, the initial GOS of each sample is the largest, indicating that the corresponding ferrite grains have the highest residual plastic strain (Figure 10(b)). Figure 10(c) shows that the stress state has a significant influence on the GOS evolution of samples. For the shear sample, GOS increased significantly when the grain size is 3 to 5 μm, while GOS increment decreased after the grain size continued to increase (Figure 8(c)). However, the GOS values of the uniaxial tensile and plane strain samples monotonically

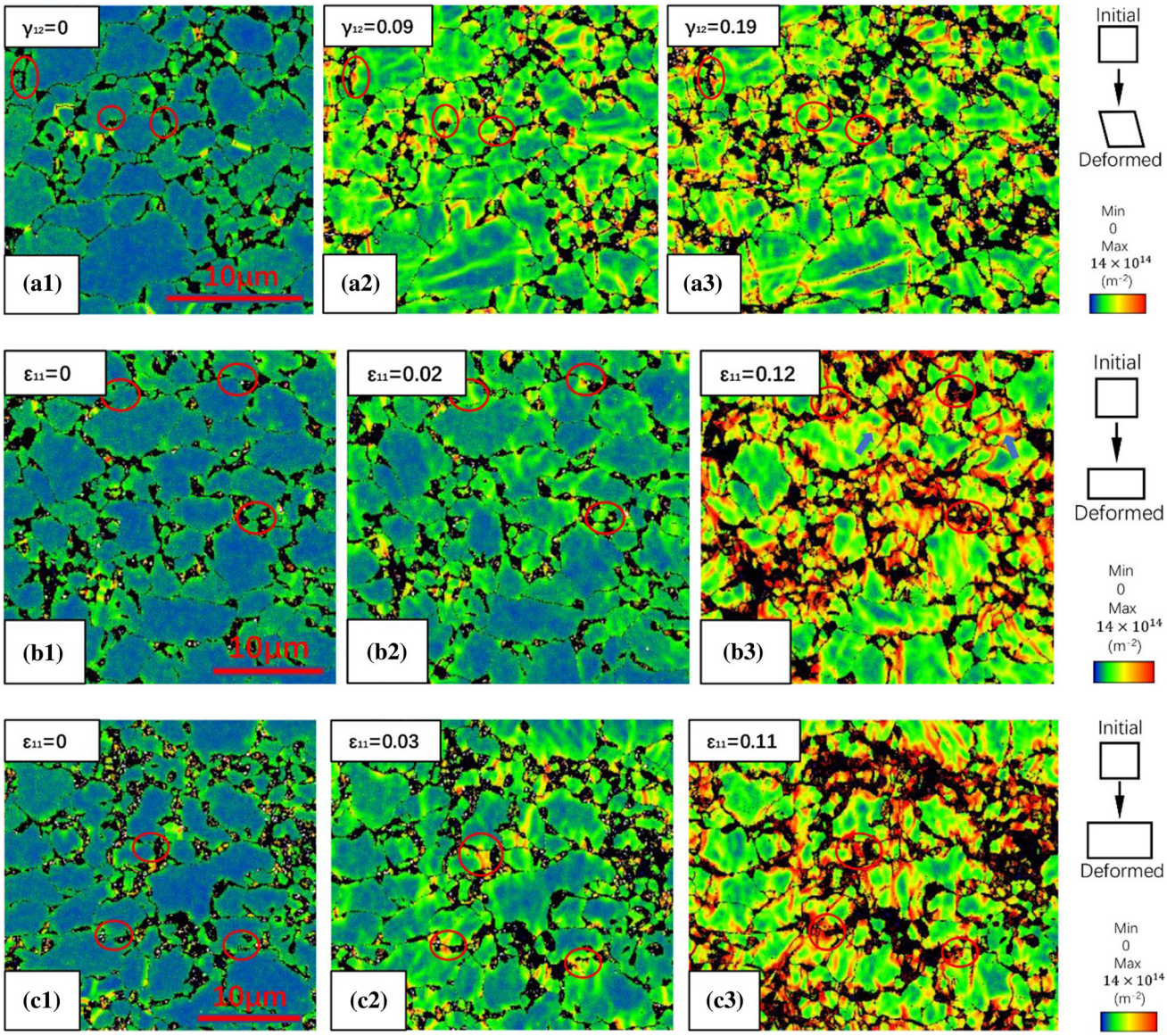

Fig. 7—The evolution maps of GND of each sample and the deformation schematic diagram of the observed area. (*a1*), (*a2*), and (*a3*) are the GND maps of the shear sample in the undeformed stage, deformed stage 1 and deformed stage 2, respectively; (*b1*), (*b2*), and (*b3*) are the GND maps of the uniaxial tensile sample in the undeformed stage, deformed stage 1 and deformed stage 2, respectively; (*c1*), (*c2*), and (*c3*) are the GND maps of the plane strain sample in the undeformed stage, deformed stage 1 and deformed stage 2, respectively.

increase with increasing grain size. In addition, Figure 10(d) shows that when the grain size is larger than 3 μm, the GOS values of all the grains are similar, indicating that the grain deformation in the shear condition is uniform. In contrast, the strains of the uniaxial tensile and plane strain samples are more concentrated in large-size grains with the increase of the deformation (Figures 10(e) and (f)).

In addition, under similar equivalent strain condition, the intragranular deformation of the grains is uniform (the IPF within a single grain is similar after deformation) in the shear sample and is heterogeneous in the uniaxial tensile and plane strain samples (the large grains are decomposed into many subgrains), as shown in Figure 11. The significant difference in intragranular IPF (Figures 11(b) and (c)) indicates that the tensile load exacerbates the heterogeneity of intragranular deformation of DP steel. Figure 12 shows the evolution of the IPF of each sample with the macro-deformation. As the macroscopic strain increases, the orientation of each grain is adjusted, and the intragranular misorientation increases significantly. In contrast, the intragranular orientation divergence is most pronounced in uniaxial tensile and plane strain samples.

Table III. The von-Mises Equivalent Strains of All Samples

	Shear		Uniaxial Tension		Plane Strain	
Deformation\Stress State	Shear Strain	E-Strain	Tensile Strain	E-Strain	Tensile Strain	E-Strain
Undeformed Stage	0	0	0	0	0	0
Deformation Stage 1	0.09	0.073	0.02	0.02	0.03	0.035
Deformation Stage 2	0.19	0.11	0.12	0.12	0.11	0.126

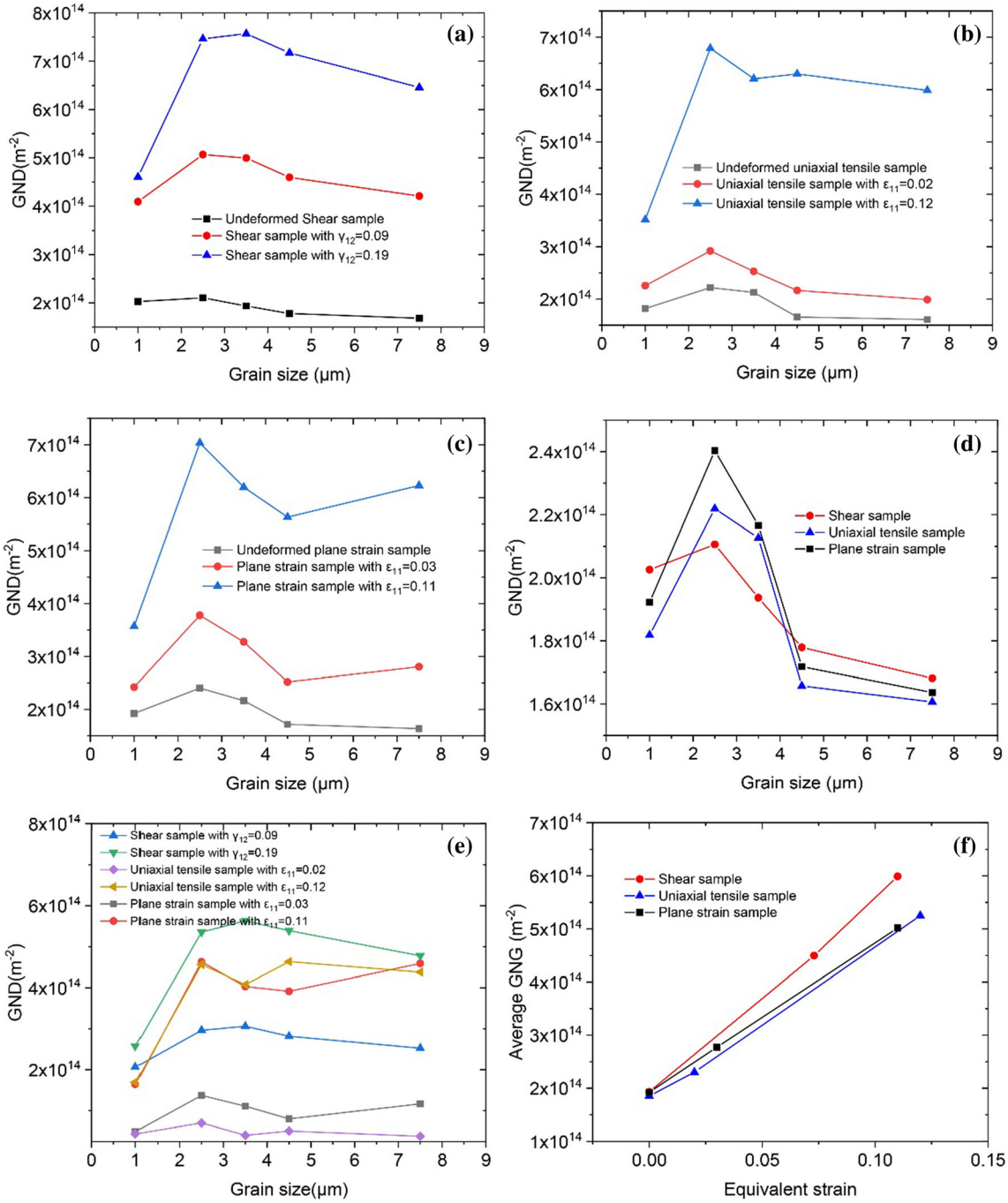

Fig. 8—Effect of grain size and deformation on average GND density of ferrite. (*a*) the shear sample; (*b*) the uniaxial tensile sample; (*c*) the plane strain sample; (*d*) the initial GND density of three samples; (*e*) GND density of three samples caused by deformation; (f) average GND-equivalent strain curves under different stress states.

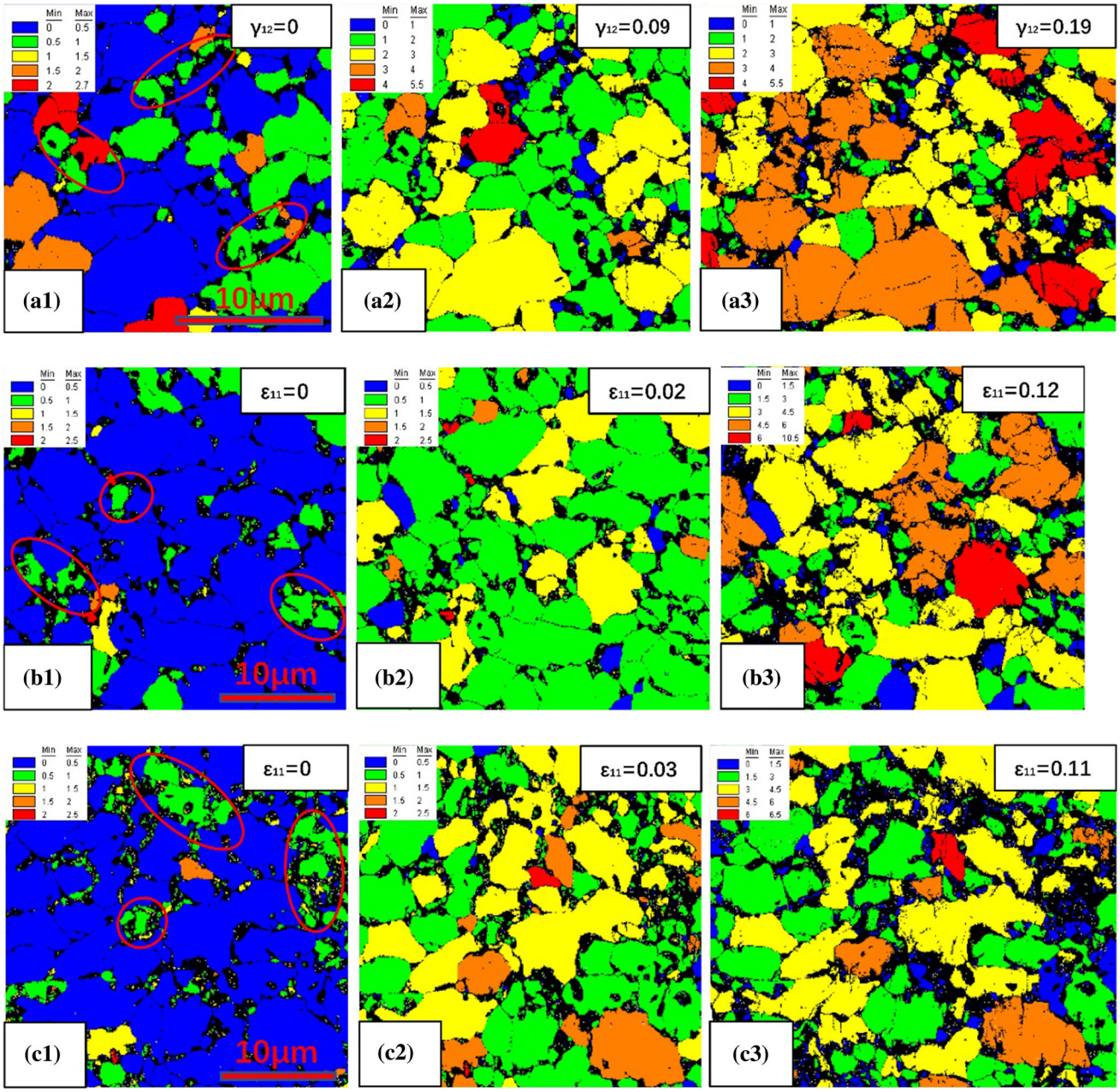

Fig. 9—The GOS maps of various stress state samples. (*a1*), (*a2*), and (*a3*) are the GOS maps of the shear sample in the undeformed stage, deformed stage 1 and deformed stage 2, respectively; (*b1*), (*b2*), and (*b3*) are the GOS maps of the uniaxial tensile sample in the undeformed stage, deformed stage 1 and deformed stage 2, respectively; (*c1*), (*c2*), and (*c3*) are the GOS maps of the plane strain sample in the undeformed stage, deformed stage 1 and deformed stage 2, respectively.

IV. CONCLUSION

In this work, the grain deformation and hardening behavior of high-strength DP steel under various stress states were studied experimentally. Based on the high-resolution EBSD system, we first analyzed the effect of MTAP on the distribution of ferrite residual deformation after annealing and its initial hardening. Then, the distribution features of GND and the influence of grain size on the evolution of GND under three stress states were analyzed. Finally, the deformation of ferrite under three stress conditions were studied. Based on the above discussion, the following conclusions can be drawn:

(1) The residual deformation after annealing of ferrite caused by MTAP depends on the martensite distribution and ferrite grain size. The residual plastic deformation in fine ferrite grains adjacent to the martensite group is the largest

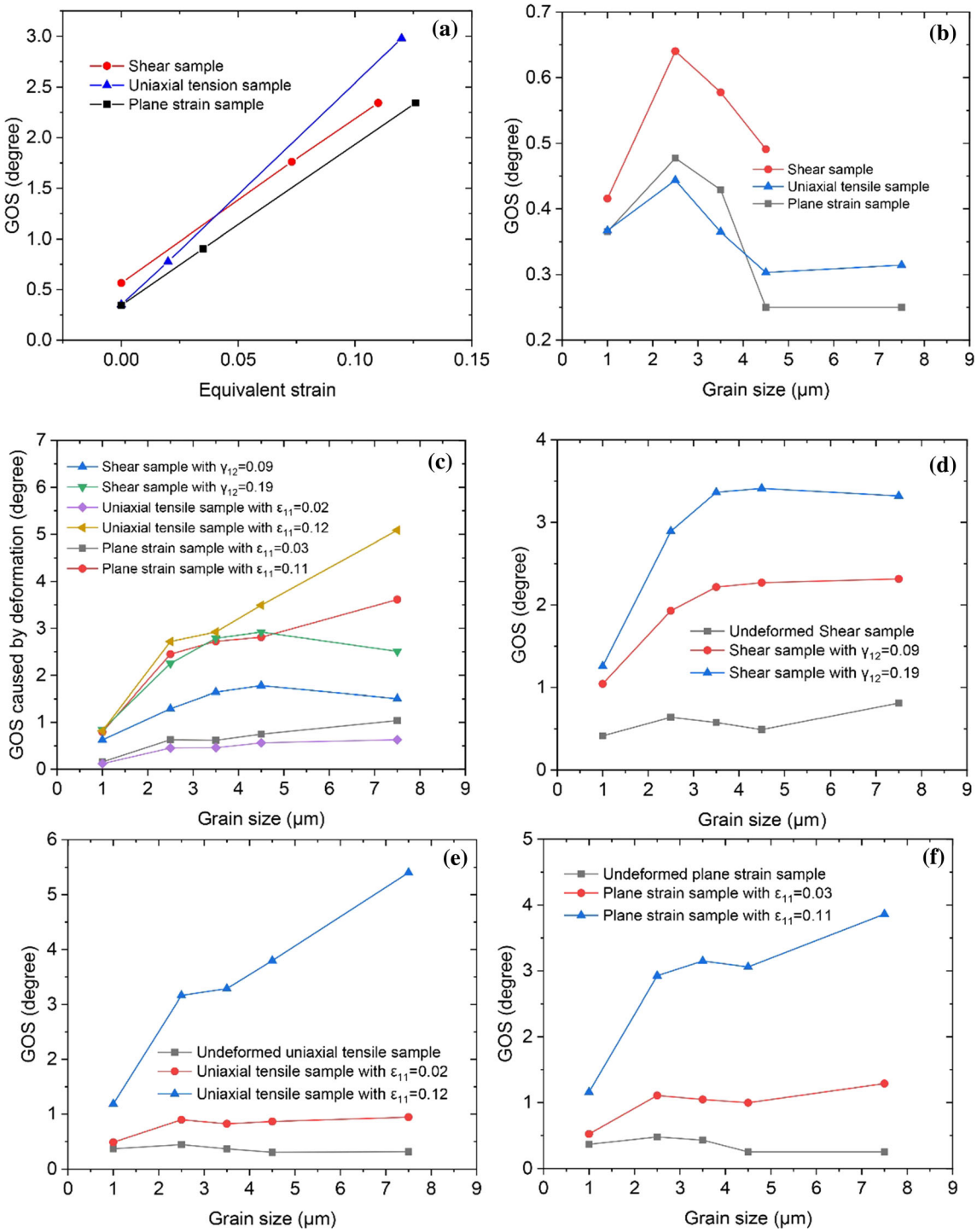

Fig. 10—The effect of grain size and deformation on GOS of ferrite. (*a*) Average GOS-equivalent strain curves under different stress states; (*b*) the initial GOS of three samples; (*c*) GOS of three samples caused by deformation; (*d*) to (*f*) are the GOS-grain size curves of shear sample, uniaxial tensile sample and plane strain sample, respectively.

and decreases with the increase in distance from the phase boundary in the large-size ferrite. In addition, MTAP has little effect on the initial GND distribution of ferrite grains.

(2) The stress state has a significant effect on the distribution of GND caused by the deformation. The high-density bands of the shear sample are consistent with the shear stress (strain) direction, and the high-density GND bands of the uniaxial tensile and plane strain samples are perpendicular to their stretching directions. In addition, the initial average GND density is related to the grain size, and the GND density of the grains is the highest when the grain size is 2 to 3 μm. However,

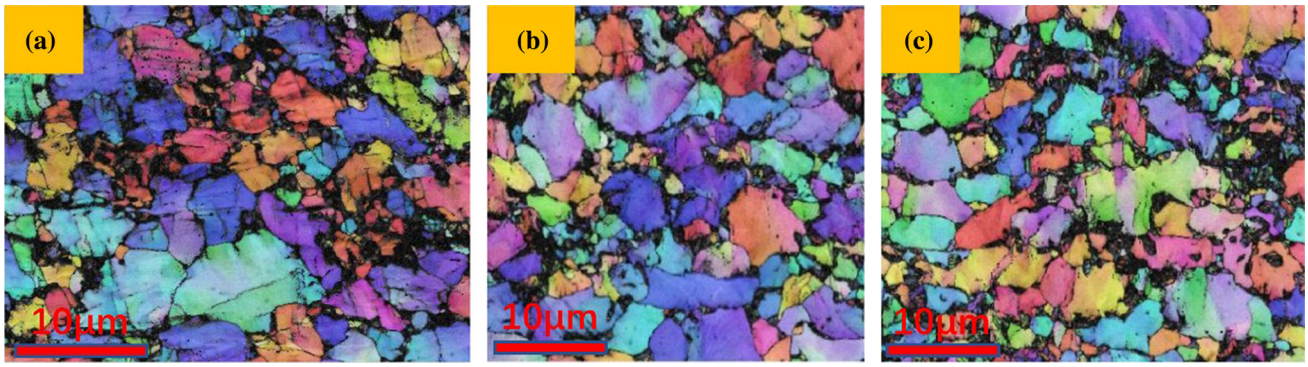

Fig. 11—The IPF-Z maps of deformed samples. (*a*) The shear sample with $\gamma_{11} = 0.19$; (*b*) the uniaxial tensile sample with $\varepsilon_{11} = 0.12$; (*c*) the plane strain sample with $\varepsilon_{11} = 0.11$.

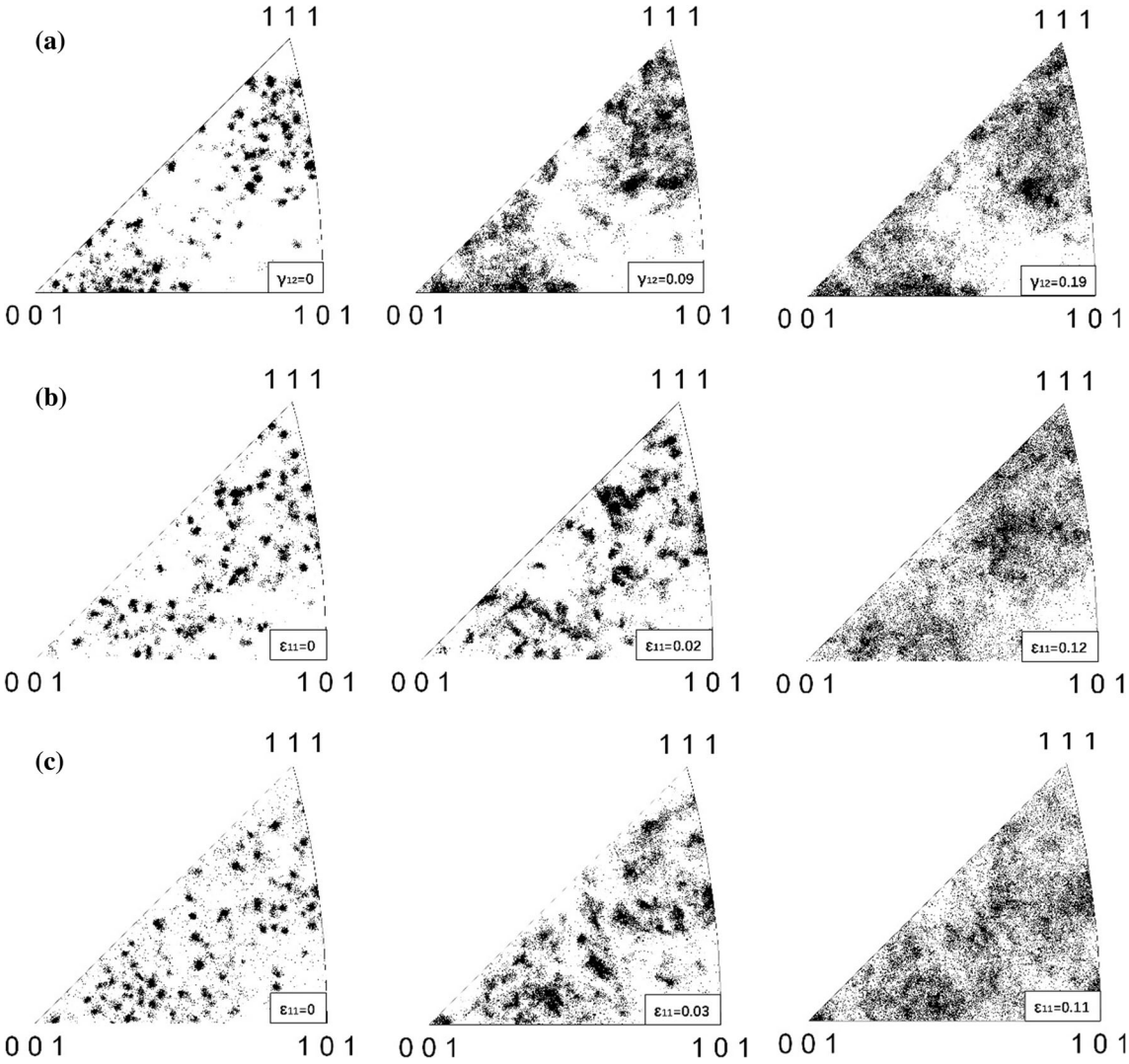

Fig. 12—The IPF-Z of various stress state samples. (*a*) The shear sample; (*b*) the uniaxial tensile sample; (*c*) the plane strain sample.

the deformation-induced GND is independent of the grain size and depends on the stress state.

(3) The inhomogeneity deformation of ferrite grains is significant and is related to the stress state. The ferrite deformation of the DP steel in the shear condition is uniform and has little correlation with the grain size. However, the deformation of the uniaxial tensile and plane strain samples tends to aggregate in large-size grains. The average GOS in the micro-region is linearly related to the equivalent strain of the samples, and its slope is related to the stress state.

REFERENCES

1. K. Hulka: *Mater. Sci. Forum*, 2003, vol. 414, pp. 101–10.
2. P. Tsipouridis, E. Werner, C. Krempaszky, and E. Tragl: *Steel Res. Int*., 2006, vol. 77 (9-10), pp. 654–67.
3. K. Mukherjee, S. Hazra, P. Petkov, and M. Militzer: *Mater. Manuf. Processes*, 2007, vol. 22 (4), pp. 511–515.
4. C. Chang: Correlation between the Microstructure of Dual Phase Steel and Industrial Tube Bending Performance, University of Windsor, 2010, pp. 7–14.
5. G.R. Speich and R.L. Miller: *Structure and Properties of Dual-Phase Steels*, R.A. Kot and J.W. Morris, eds., TMS-AIME, Warrendale, Pennsylvania, 1979, pp. 145–82.
6. A. López-Baltazar, A. Salinas-Rodríguez, and E. Nava-Vázquez: *Mater. Sci. Forum*, 2007, vol. 560, pp. 79–84.
7. P.R. Mould: *JOM*, 1982, vol. 34 (5), pp. 18–28.
8. Z. Zhang, R. Song, Z. Cheng, A. Zhao, Z. Zhao, G. Liu, and A. Xiong: *Hot Work. Technol*., 2008, vol. 37 (6), pp. 27–33.
9. S. Renbo, G. Zhifei, and D. Qifeng: International Conference on Steel Rolling, 2010.
10. A. Ramazani, K. Mukherjee, A. Schwedt, P. Goravanchi, U. Prahl, and W. Bleck: *Int. J. Plast*., 2013, vol. 43, pp. 128–52.
11. M. Calcagnotto, D. Ponge, E. Demir, and D. Raabe: *Mater. Sci. Eng.: A*, 2010, vol. 527 (10–11), pp. 2738–46.
12. P. Tsipouridis: Mechanical properties of dual-phase steels, Technical University, Muenchen, Germany, 2006.
13. G.T. Hahn: *Acta Metall*., 1962, vol. 10 (8), pp. 727–38.
14. S.S. Hansen and R.R. Pradhan: in *Fundamentals of Dual-Phase Steels*, R.A. Kot and B.L. Bramfitt, eds., TMS-AIME, Warrendale, 1981, pp. 113–44.
15. J. Kang, Y. Ososkov, J.D. Embury, and D.S. Wilkinson: *Scr. Mater*., 2007, vol. 56 (11), pp. 999–1002.
16. H. Ghadbeigi, C. Pinna, S. Celotto, and J.R. Yates: *Mater. Sci. Eng.: A*, 2010, vol. 527 (18–19), pp. 5026–32.
17. C.C. Tasan, J.P.M. Hoefnagels, and M.G.D. Geers: *Scr. Mater*., 2010, vol. 62 (11), pp. 835–38.
18. C.C. Tasan, J.P. Hoefnagels, M. Diehl, D. Yan, F. Roters, and D. Raabe: *Int. J. Plast*., 2014, vol. 63, pp. 198–210.
19. C.C. Tasan, M. Diehl, D. Yan, C. Zambaldi, P. Shanthraj, F. Roters, and D. Raabe: *Acta Mater*., 2014, vol. 81, pp. 386–400.
20. D. Yan, C.C. Tasan, and D. Raabe: *Acta Mater*., 2015, vol. 96, pp. 399–409.
21. G.I. Taylor: *J. Inst. Met*., 1938, vol. 62, pp. 307–24.
22. G.I. Taylor: *Proc. R. Soc. Lond. Ser. A*, 1934, vol. 145 (855), pp. 362–87.
23. H. Ghassemi-Armaki, R. Maaß, S.P. Bhat, S. Sriram, J.R. Greer, and K.S. Kumar: *Acta Mater*., 2014, vol. 62, pp. 197–211.
24. J. Kadkhodapour, S. Schmauder, D. Raabe, S. Ziaei-Rad, U. Weber, and M. Calcagnotto: *Acta Mater*., 2011, vol. 59 (11), pp. 4387–94.
25. M.F. Ashby: *Philos. Mag.: J. Theor. Exp. Appl. Phys*., 1970, vol. 21 (170), pp. 399–424.
26. J.F. Nye: *Acta Metall*., 1953, vol. 1 (2), pp. 153–162.
27. S. Sinha, J.A. Szpunar, N.K. Kumar, and N.P. Gurao: *Mater. Sci. Eng.: A*, 2015, vol. 637, pp. 48–55.
28. X. Zhao, Y. Fan, H. Wang, and Y. Liu: *Mater. Lett*., 2015, vol. 160, pp. 51–54.
29. M.A. Mohtadi-Bonab and M. Eskandari: *Eng. Fail. Anal*., 2017, vol. 79, pp. 351–60.
30. A. Kundu and D.P. Field: *Mater. Sci. Eng.: A*, 2016, vol. 667, pp. 435–43.
31. *Electron Backscatter Diffraction in Materials Science*, ed., A.J. Schwartz, and M. Kumar, and B.L. Adams, and D.P. Field, eds., *Electron Backscatter Diffraction in Materials Science*, Springer, New York, 2009.
32. M. Kamaya: *Mater. Charact*., 2009, vol. 60 (2), pp. 125–132.
33. S.I. Wright, M.M. Nowell, and D.P. Field: *Microsc. Microanal*., 2011, vol. 17 (3), pp. 316–29.
34. M. Kamaya, A.J. Wilkinson, and J.M. Titchmarsh: *Nuclear Eng. Des*., 2005, vol. 235 (6), pp. 713–25.
35. A. Sáez-Maderuelo, L. Castro, and G. De Diego: *J. Nuclear Mater*., 2011, vol. 416 (1–2), pp. 75–79.

Publisher's Note Springer Nature remains neutral with regard to jurisdictional claims in published maps and institutional affiliations.